ACS APPLIED MATERIALS & INTERFACES
Research Article
www.acsami.org

Highly Porous $NiCo_2O_4$ Nanoflakes and Nanobelts as Anode Materials for Lithium-Ion Batteries with Excellent Rate Capability

Anjon Kumar Mondal,* Dawei Su, Shuangqiang Chen, Xiuqiang Xie, and Guoxiu Wang*

Centre for Clean Energy Technology, School of Chemistry and Forensic Science, University of Technology, Sydney, Broadway, Sydney, NSW 2007, Australia

Supporting Information

ABSTRACT: Highly porous $NiCo_2O_4$ nanoflakes and nanobelts were synthesized by using a hydrothermal technique, followed by calcination of the $NiCo_2O_4$ precursors. The as-synthesized materials were analyzed by scanning electron microscopy, X-ray diffraction, transmission electron microscopy, and Brunauer–Emmett–Teller methods. The $NiCo_2O_4$ nanoflakes and nanobelts were applied as anode materials for lithium-ion batteries. Owing to the unique porous structural features, the $NiCo_2O_4$ nanoflakes and nanobelts exhibited high specific capacities of 1033 and 1056 mA h g^{-1}, respectively, and good cycling stability and rate capability. These exceptional electrochemical performances could be ascribed to the remarkable structural feature with a high surface area and void spaces within the surface of nanoflakes and nanobelts, which provide large contact areas between electrolyte and active materials for electrolyte diffusion and cushion the volume variation during the lithium-ion insertion/extraction process.

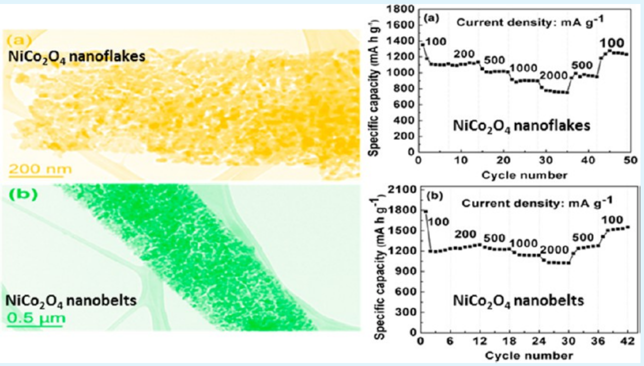

KEYWORDS: *$NiCo_2O_4$ nanoflakes, $NiCo_2O_4$ nanobelts, hydrothermal method, lithium-ion battery, electrochemical performance*

1. INTRODUCTION

The limited traditional energy resources and the increasing concerns on environmental pollution are major driving forces for the development of sustainable and clean energy sources.[1−3] As one of the most promising energy storage devices, the lithium-ion batteries have progressively attracted extensive interests within the industrial and scientific communities. It is now the dominate power source for portable electronics and electric/hybrid electric cars.[4−6] The ever-increasing energy demand has inspired current research to develop new high-performance electrode materials with various morphologies, from micro to nanoscales, for lithium-ion batteries. Owing to their higher theoretical specific capacity (500−1000 mA h g^{-1}) and reversible conversion mechanism for lithium storage, nanostructured transition metal oxides have been considered as a possible alternative anode material for lithium-ion batteries.[7−12,43,44] However, poor cycling performance and low electrical conductivity limit their practical application. Among transition metal oxides, cobalt oxide exhibited capacity 3 times higher than that of conventional graphite; however, because of the high cost and toxic nature of cobalt, it has not been recognized as an alternative anode material. Many efforts have been devoted to partially replacing cobalt oxide with other inexpensive and environmentally friendly metal oxides.[13−16]

Binary metal oxides, such as $CuCo_2O_4$, $MnCo_2O_4$, $ZnCo_2O_4$, $NiCo_2O_4$, and $ZnMn_2O_4$, have also been reported as anode materials for lithium-ion batteries.[13−17] Among different binary metal oxides, $NiCo_2O_4$ is a very promising electrode material because of its high theoretical capacity (890 mA h g^{-1}). More importantly, it has been reported that $NiCo_2O_4$ has much higher electrical conductivity and electrochemical performances than nickel oxides and cobalt oxides.[18] The higher electronic conductivity is favorable for the rapid transfer of electrons in an electrode. Because of the synergistic effect from higher electronic conductivity and porous structure, $NiCo_2O_4$ nanoflakes and nanobelts show much better electrochemical performances than nickel oxide and cobalt oxide. Owing to its intriguing properties, it emerges as a promising material for diverse applications, such as photodetectors,[19] electrocatalytic water splitters,[20] supercapacitors,[21] and lithium-ion batteries.[16,22] In order to develop high-performance lithium-ion batteries, electrode materials play a very important role in terms in determining the performance of batteries. Generally, porous electrode materials exhibit several beneficial properties, which are preferable for the enhancement of electrochemical performances; these include that (i) the porous structure can offer space for volume change throughout the cycling process, and (ii) the high specific surface area can greatly improve the interface contact between the active materials and electrolyte, facilitating fast Li^+ and electron transport.[23,24] It is also well-recognized that the rate performance of electrode materials is generally determined by electronic conductivity and the kinetics

Received: March 1, 2014
Accepted: August 13, 2014
Published: August 13, 2014

of ion diffusion. Thus, the design of electrode materials with different shapes and sizes is essential to improve electrochemical performances of lithium-ion batteries. $NiCo_2O_4$ has been widely studied as an electrode material for supercapacitors owing to its remarkable electrical conductivity and electrochemical activities.[25−28] However, there have been only a few reports on the application of $NiCo_2O_4$ as anode materials for lithium-ion batteries. Qian et al. have reported monodisperse $NiCo_2O_4$ mesoporous microspheres by a solvothermal method with subsequent annealing of the precursor, which displayed good battery performance.[16] Porous flower-like $NiCo_2O_4$ was synthesized through a hydrothermal method, followed by calcination in air. The flower-like $NiCo_2O_4$ exhibited improved lithium storage properties and good cycling performance.[22] Li and co-workers have fabricated well-aligned nanorod arrays on Cu substrates via a one-pot hydrothermal decomposition, followed by annealing in air. The nanorod arrays demonstrated higher lithium storage performances.[29]

Herein, we reported the preparation of highly porous $NiCo_2O_4$ nanoflakes and nanobelts by a simple template-free hydrothermal method. The as-prepared $NiCo_2O_4$ nanostructures demonstrated high specific capacity, excellent rate capability, and a good cycling stability.

2. EXPERIMENTAL SECTION

2.1. Synthesis of $NiCo_2O_4$ Nanoflakes and Nanobelts.

In a typical synthesis process of $NiCo_2O_4$ nanoflakes, 0.687 mmol of $Ni(NO_3)_2{\cdot}6H_2O$ and 1.375 mmol of $Co(NO_3)_2{\cdot}6H_2O$ are dissolved in 25 mL of deionized (DI) water, followed by the addition of 0.516 g of glycine and 0.585 g of Na_2SO_4 salt. The mixture was slowly adjusted to pH 11 by the dropwise addition of 5 M NaOH solution and stirred for 1 h. The resultant mixture was transferred into a 30 mL Teflon-lined stainless steel autoclave and heated at 180 °C for 20 h. After cooling to room temperature, the precipitates were collected by filtration, washed with DI water and ethanol, and dried in a vacuum oven at 80 °C for 12 h. Finally, to obtain the porous nanoflakes, the precursor was annealed at 500 °C for 3 h in air. For the synthesis of $NiCo_2O_4$ nanobelts, the process was almost identical to the synthesis of $NiCo_2O_4$ nanoflakes described above. The only difference is the addition of 50% ethanol and 50% water instead of 100% water.

2.2. Materials Characterization.

The as-synthesized $NiCo_2O_4$ nanoflakes and nanobelts were characterized using a GBC MMA X-ray diffractometer (λ = 0.15405 nm), a field emission scanning electron microscope (FESEM, Zeiss Supra 55VP) with an energy-dispersive X-ray (EDX) attachment, and a transmission electron microscope (TEM, JEOL 2011 TEM facility). The specific surface area was calculated using the Brunauer−Emmett−Teller (BET) method. The pore size distribution and average pore diameter were calculated by the Barrett−Joyner−Halenda (BJH) equation using a Micromeritics 3 Flex surface characterization analyzer at 77 K. Fourier transform infrared (FTIR) spectroscopy was performed on a Bruker Tensor 27 IR spectrometer using KBr as dispersant between 400 to 4000 cm^{-1}. Thermogravimetric analysis (TGA) was carried out at a heating rate of 10 °C min^{-1} from room temperature to 600 °C with an air flow rate of 30 mL min^{-1} by using the 2960 SDT thermal analyzer.

2.3. Electrochemical Measurements.

The electrochemical performances of the as-prepared $NiCo_2O_4$ nanoflakes and nanobelts were measured under room temperature by using coin cells (CR 2032), in which lithium was used as the counter electrode as well as the reference electrode. The working electrode was prepared using the active material ($NiCo_2O_4$ nanobelts and nanoflakes), acetylene carbon black (conductive agent), and polyvinylidene fluoride (PVDF) binder in a weight ratio of 60:20:20. The slurry was pasted onto a copper foil substrate (area of loading: 1 cm^2, and a total mass of around 1 mg) and dried in a vacuum oven at 100 °C overnight. A thin round sheet of microporous polythene (Celgard 2400) was used as separator, and 1 M $LiPF_6$ in ethylene carbonate (EC) and diethyl carbonate (DEC) (1:1 by volume) was used as the electrolyte (20 μL for each cell). The cells were assembled in an argon-filled glovebox (UniLab, MBRAUN, Germany) with water and oxygen contents of less than 1 ppm. The galvanostatic charge−discharge cycling was evaluated by the NEWARE-BTS battery tester with a potential window of 0.01−3.0 V. The cyclic voltammetry (CV) experiment was carried out using a CHI 660C electrochemistry workstation in the voltage range of 0.01−3.0 V (vs Li^+/Li) and at a scan rate of 0.1 mV s^{-1}. Electrochemical impedance spectroscopy (EIS) was conducted on the CHI 660C electrochemistry workstation in the frequency range from 0.1 MHz to 0.01 Hz.

3. RESULTS AND DISCUSSION

The crystalline structure and phase purity of the $NiCo_2O_4$ materials were characterized by XRD. Figure 1a,b shows the XRD patterns of $NiCo_2O_4$ nanoflakes and nanobelts. Nine distinct diffraction peaks are observed at 2θ values of 19.3, 31.2, 36.8, 38.5, 44.8, 55.8, 59.3, 65.2, and 77.2°, respectively (Figure 1a). All of these diffraction peaks can be indexed to (111), (220), (311), (222), (400), (422), (511), (440), and (533) crystal planes and assigned to cubic $NiCo_2O_4$ with a spinel crystalline structure (JCPDS card no. 73-1702). In Figure 1b, the small peak at around 74° can be indexed to the (620) crystal plane of $NiCo_2O_4$. All diffraction peaks in Figure 1b can also be ascribed to the cubic $NiCo_2O_4$ with a spinel crystalline structure (JCPDS card no. 73-1702).[25] No other impurity peaks were observed, which indicates that the pure $NiCo_2O_4$ nanoflakes and nanobelts were formed after thermal treatment.

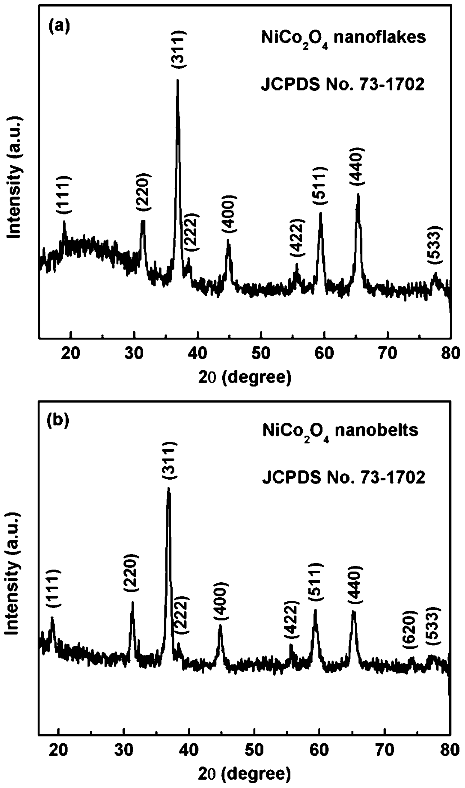

Figure 1. XRD patterns of $NiCo_2O_4$ calcinated at 500 °C for 3 h: (a) nanoflakes and (b) nanobelts.

The morphologies of the as-synthesized Ni-Co based intermediate products and $NiCo_2O_4$ nanoflakes and nanobelts were determined by FESEM. Figure S1a,b (Supporting Information) shows the SEM images of Ni-Co based

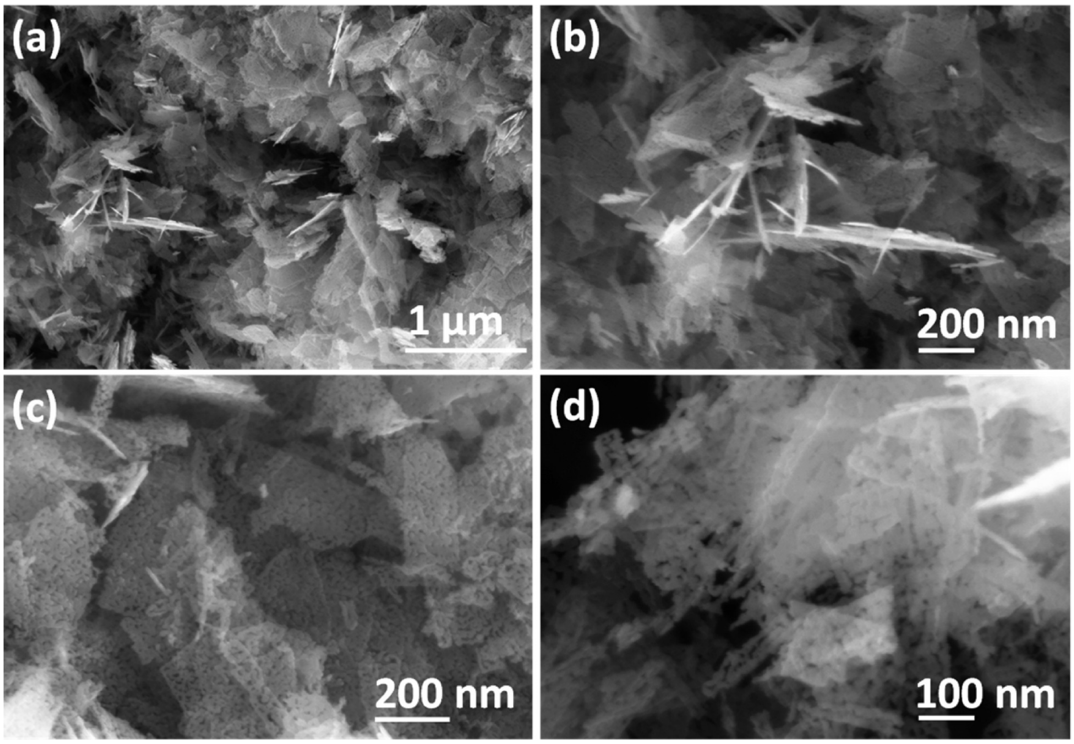

Figure 2. FESEM images of porous $NiCo_2O_4$ nanoflakes: (a, b) low magnification and (c, d) high magnification.

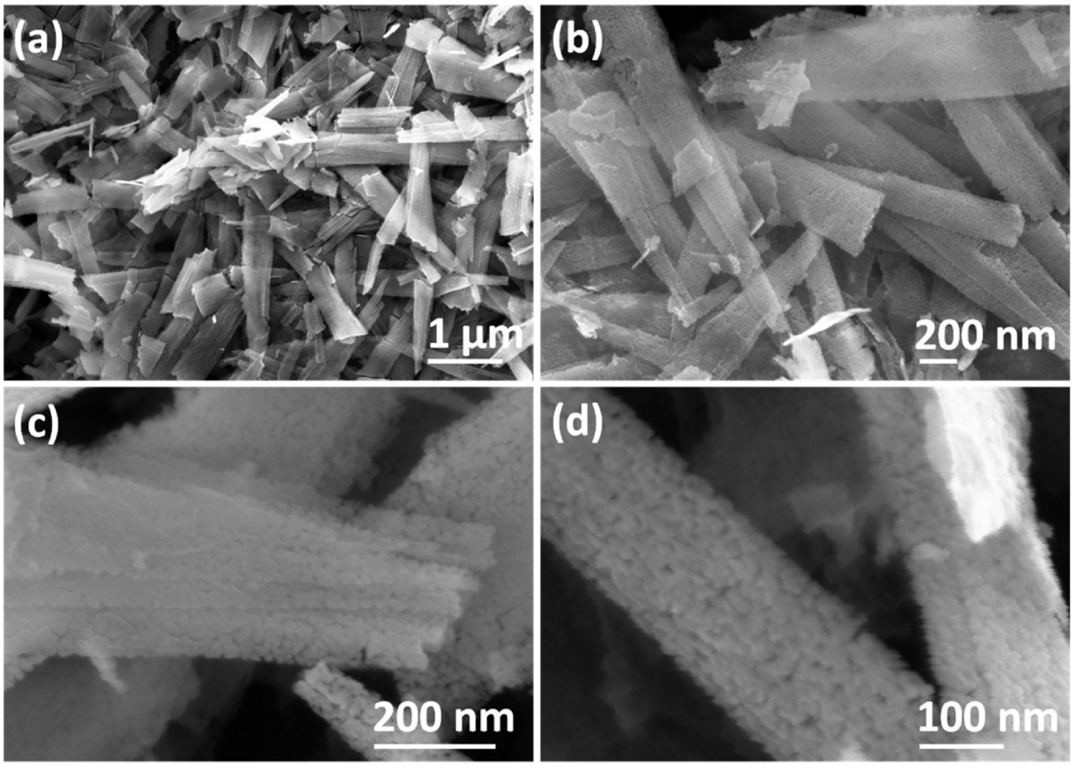

Figure 3. FESEM images of porous $NiCo_2O_4$ nanobelts: (a, b) low magnification and (c, d) high magnification.

intermediate products (nanoflakes). From the low- and high-magnification images, the uniform distribution of nanoflakes is observed. Figure S1c,d shows the nanobelts of the Ni-Co based intermediate with a regular distribution. Remarkably, the nanoflake and nanobelt structures were maintained even after thermal treatment of the precursors. There is no obvious morphology change, which demonstrates excellent structural stability (Figures 2 and 3). Figure 2 displays different magnification SEM images of $NiCo_2O_4$ nanoflakes. From the low-magnification SEM images, a uniform distribution of $NiCo_2O_4$ nanoflakes is observed (Figure 2a,b). The high-magnification SEM images show the nanoflake structure with

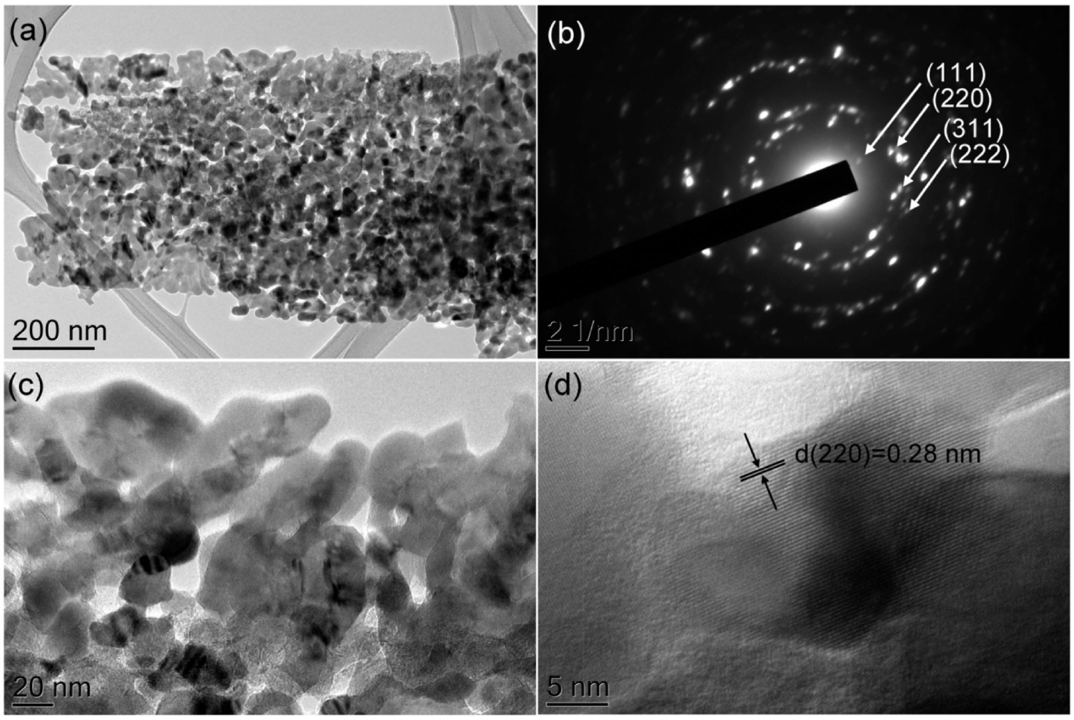

Figure 4. (a) Low-magnification TEM image of $NiCo_2O_4$ nanoflakes, (b) its corresponding selected area electron diffraction patterns (SAED), (c) high-magnification TEM image, and (d) lattice resolved HRTEM image.

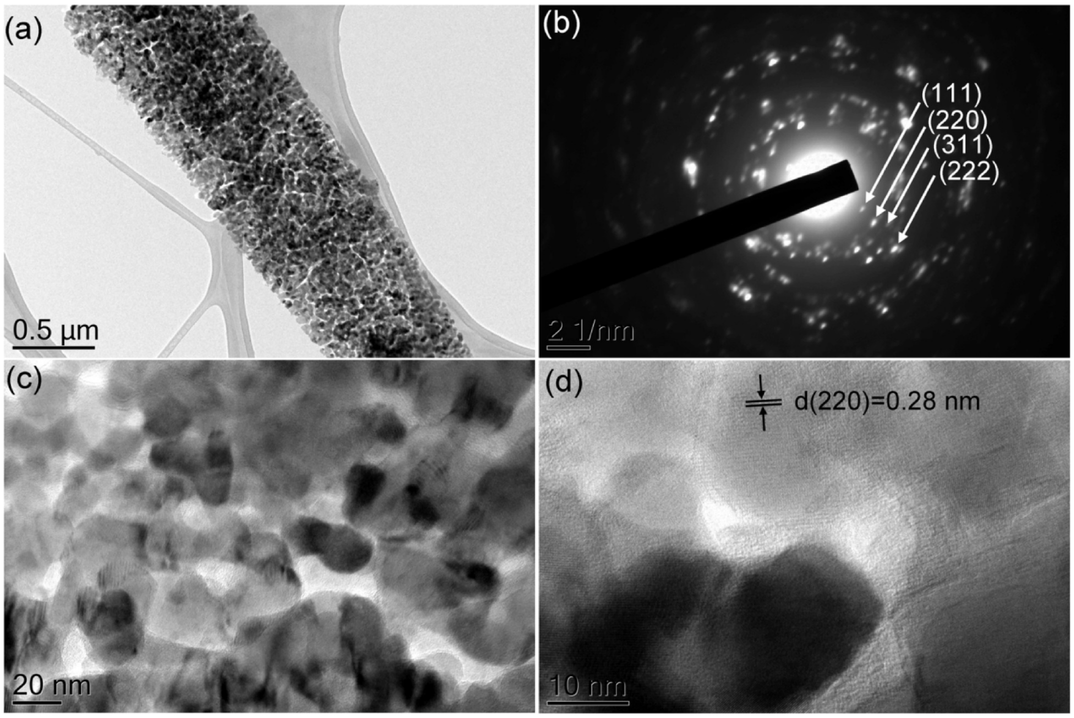

Figure 5. (a) Low-magnification TEM image of $NiCo_2O_4$ nanobelts, (b) its corresponding selected area electron diffraction patterns (SAED), (c) high-magnification TEM image, and (d) lattice resolved HRTEM image.

clearly visible small pores on the surface of nanoflakes (Figure 2c,d). Figure 3a,b shows the low-magnification SEM images of $NiCo_2O_4$ nanobelts, in which nanobelts are homogeneously distributed. From the high-magnification SEM images, we can clearly observe that there are many mesopores on the surface of the nanobelts (Figure 3c,d).

We investigated the morphology development of Ni-Co based precursors and $NiCo_2O_4$ nanoflakes and nanobelts. Strong alkaline conditions and the presence of glycine were essential for the growth of nanoflakes and nanobelts. In the absence of glycine and without alkaline conditions, nanoparticles were formed. Glycine is applied as a hydrolysis controlling agent for the formation of $NiCo_2O_4$ nanoflakes and nanobelts. Assisted by amphiphilic glycine, the $NiCo_2O_4$ precursors tend to form a layered structure, which was uniformly wrapped by the hydrophobic part of glycine. Meanwhile, the hydrophilic part of glycine was dissolved in the aqueous solution. Through the hydrolysis of glycine during the hydrothermal process, more OH^- ions generate in the solution and the pH value of the solution significantly increases, leading to the formation of a nanoflake or nanobelt structure rather than nanoparticles. The temperature also has a significant effect on morphology development. The nanoflakes and nanobelts were not achieved if the temperature is less than 180 °C. When the temperature is increased to 200 °C, the similar morphology of nanoflakes and nanobelts can be obtained. The Ni-Co based precursors are calcined at 500 °C for 3 h to obtain porous $NiCo_2O_4$ nanoflakes and nanobelts. The surface compositions of $NiCo_2O_4$ nanoflakes and nanobelts were also determined by energy-dispersive X-ray spectroscopy (EDX), which confirms the presence of Ni, Co, and O atoms (Figure S2, in the Supporting Information). The peaks of carbon originated from the C substrate.

We further used transmission electron microscopy (TEM) and selected-area electron diffraction (SAED) patterns to identify the microstructure of as-prepared $NiCo_2O_4$ nanoflakes and nanobelts, as shown in Figures 4 and 5, respectively. In Figure 4a, it can be clearly seen that, in general, the product is mainly flakes with the size of ~500 nm. In the low-magnification TEM image of $NiCo_2O_4$ nanobelts (Figure 5a), the nanobelt feature of the as-prepared $NiCo_2O_4$ can be observed. All the selected area electron diffraction (SAED) pattern rings (Figures 4b and 5b) taken from the corresponding single $NiCo_2O_4$ nanoflake and $NiCo_2O_4$ nanobelt can be readily indexed to the $NiCo_2O_4$ crystal structure. The high-magnification TEM image (Figures 4c and 5c) illustrate that the as-prepared $NiCo_2O_4$ nanocrystals are consistent with the mesoporous structure. Figures 4d and 5d show the lattice resolved HRTEM images of the $NiCo_2O_4$ nanoflakes and $NiCo_2O_4$ nanobelts, respectively, in which the (220) crystal plane with a *d* spacing of 0.28 nm can be directly observed. This further confirmed the crystal structure of the as-prepared $NiCo_2O_4$.

Figure 6 shows the N_2 adsorption and desorption isotherms of $NiCo_2O_4$ nanoflakes and nanobelts. All of the isotherms in Figure 6a,b can be categorized as type IV isotherms with H1 hysteresis loops, which indicates a characteristic mesoporous structure.[30] Moreover, the BET surface areas of $NiCo_2O_4$ nanoflakes and nanobelts are calculated to be around 54 and 66 $m^2\ g^{-1}$, respectively. As shown in the insets of panels (a) and (b) in Figure 6, the mesoporous structures of $NiCo_2O_4$ nanoflakes and nanobelts are further confirmed by the Barrett−Joyner−Halenda (BJH) pore size distribution data. The pore size distributions are relatively narrow, with most of the pores basically in the range of 3−5 nm for nanoflakes and 2−4 nm for nanobelts. Since the mesoporous feature and large surface area facilitate the Li^+ diffusion and electrode−electrolyte contacts throughout the electrochemical process, the $NiCo_2O_4$ nanoflakes and nanobelts could have enhanced electrochemical properties.

Thermogravimetric analysis of Ni-Co based precursors (nanoflakes and nanobelts) was carried out between room temperature and 600 °C. As illustrated in Figure S3a,b (Supporting Information), the 3.5% weight loss that occurs before 286 °C can be ascribed to the dehydration of Ni-Co based precursors. The second step (18.5% weight loss) in the TGA curves corresponds to the conversion process of Ni-Co based precursors to $NiCo_2O_4$ nanoflakes and nanobelts. In the temperature range between 500 and 600 °C, no obvious weight loss is observed, which is inferred as the thorough decomposition of the precursors, structural integrity, and absence of any other phases. Therefore, the calcination temperature of 500 °C was applied in order to achieve single phase $NiCo_2O_4$ nanoflakes and nanobelts. Figure S4 (Supporting Information) shows the FTIR spectra of $NiCo_2O_4$ nanoflakes and $NiCo_2O_4$ nanobelts. For the nanoflakes (Figure S4a), the peaks at around 662 and 565 cm^{-1} arise from the metal−oxygen (M−O) vibrations of the $NiCo_2O_4$. The bands at around 662 and 557 cm^{-1} in Figure S4b are also ascribed to the M−O vibrations of the $NiCo_2O_4$ nanobelts.[31]

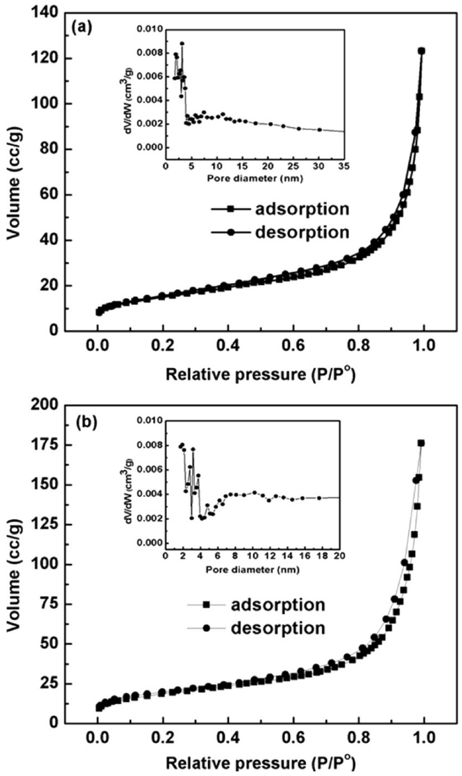

Figure 6. Nitrogen adsorption/desorption isotherms and corresponding BJH pore size distributions (inset) of (a) $NiCo_2O_4$ nanoflakes and (b) $NiCo_2O_4$ nanobelts.

The lithium storage properties of the as-synthesized $NiCo_2O_4$ nanoflakes and nanobelts were initially evaluated by cyclic voltammetry (CV). Figure 7a,b shows the first three CV curves of the $NiCo_2O_4$ nanoflakes and nanobelts. In the first cycle of $NiCo_2O_4$ nanoflakes, as shown in Figure 7a, the intense cathodic peak located at ~0.95 V results from the reduction of Co^{3+} and Ni^{2+} to metallic Co and Ni, respectively. However, the broad peak at ~0.68 V corresponds to the formation of a solid electrolyte interface (SEI) layer. The anodic peak is observed at ~2.1 V, which could be attributed to the oxidation of metallic Ni and Co to nickel oxides and cobalt oxides. In the second and third cycles, the redox peaks at ~1.17 and ~2.16 V corresponded to the reduction and oxidation of the nickel oxides and cobalt oxides.[16,22] Unlike nanoflakes, the $NiCo_2O_4$ nanobelt electrode displays three cathodic peaks in the first cycle. A small peak at ~1.17 V can be ascribed to the devastation of crystalline structure, which is clearly different from the other cycles.[22] A strong irreversible cathodic peak at

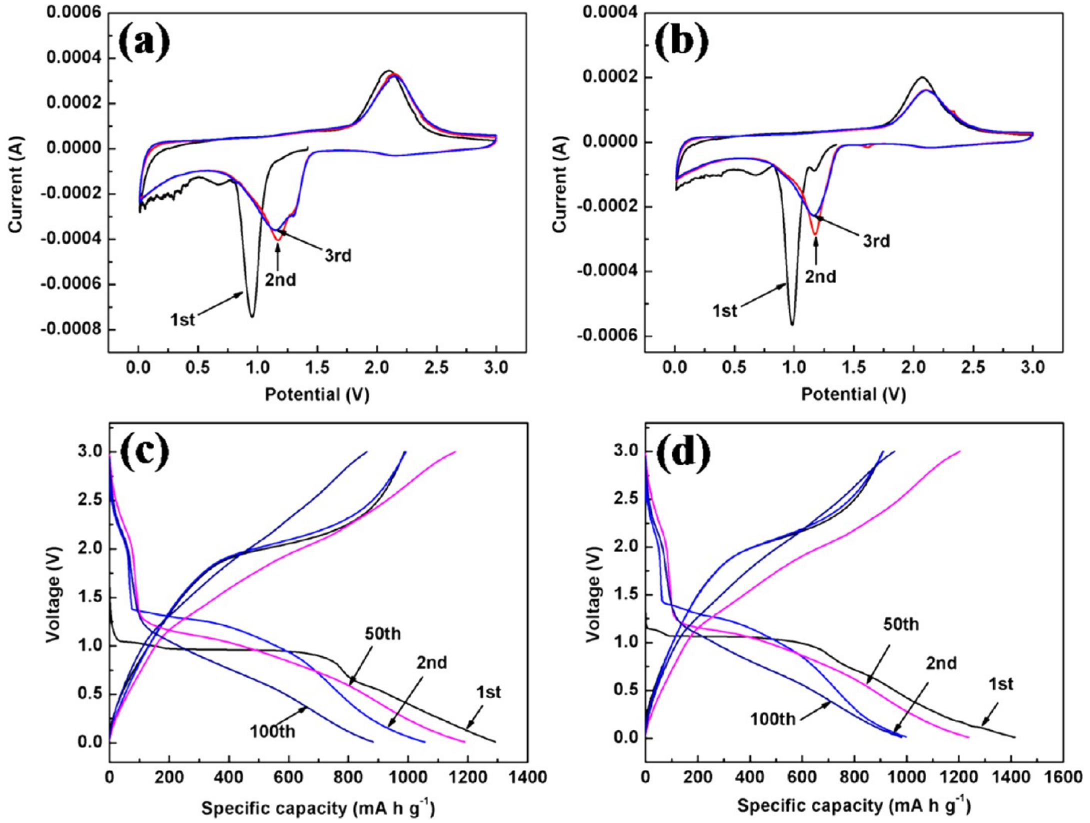

Figure 7. First three consecutive CV curves of $NiCo_2O_4$ (a) nanoflakes and (b) nanobelts at a scan rate of 0.1 mV s^{-1} in the voltage range of 0.01–3.0 V, and galvanostatic discharge and charge profiles for the 1st, 2nd, 50th, and 100th cycles of $NiCo_2O_4$ (c) nanoflakes and (d) nanobelts.

~0.99 V could be attributed to the reduction of Co^{3+} and Ni^{2+} to metallic Co and Ni, respectively. A broad peak at ~0.68 V can be attributed to the formation of SEI. The anodic peak at ~2.08 V corresponds to the oxidation of metallic Ni and Co to nickel oxides and cobalt oxides. In the subsequent cycles, the continual reduction–oxidation of NiO and CoO results in redox peaks at ~1.18 and 2.10 V, respectively. From the second cycle, there is no obvious change of the redox peaks for the $NiCo_2O_4$ nanoflake and nanobelt electrodes. This demonstrated that there is good electrochemical reversibility. On the basis of the previous reports,[16,32−34] the redox reactions can be described as follows:

$$NiCo_2O_4 + 8Li^+ + 8e^- \rightarrow Ni + 2Co + 4Li_2O \qquad (1)$$

$$Ni + Li_2O \leftrightarrow NiO + 2Li^+ + 2e^- \qquad (2)$$

$$Co + Li_2O \leftrightarrow CoO + 2Li^+ + 2e^- \qquad (3)$$

$$CoO + 1/3Li_2O \leftrightarrow 1/3Co_3O_4 + 2/3Li^+ + 2/3e^- \qquad (4)$$

The galvanostatic discharge–charge profiles of the as-prepared $NiCo_2O_4$ nanoflake and nanobelt electrodes at the current density of 500 mA g^{-1} are presented in Figure 7c,d. In the first discharge process, the $NiCo_2O_4$ nanoflake and nanobelt electrodes show a wide and steady potential plateau at 1.1 V, followed by a gradual voltage decrease. The first discharge capacity reached about 1292 and 1414 mA h g^{-1} for $NiCo_2O_4$ nanoflakes and nanobelts, respectively. The formation of a solid electrolyte interface (SEI) may contribute to the initial extra capacity at the first discharge.[16,35] The potential plateaus in the subsequent discharge curves were shifted to the higher voltage than those of the first cycle, which can be ascribed to the irreversible reaction of $NiCo_2O_4$ and Li^+ as in eq 1.[42] The consequent charge curves show a steady potential increase, which are associated with the different electrochemical mechanism. The increase of the overpotential could be ascribed to the polarization related to the ion transfer during the charge–discharge process, which is often observed in many metal oxides.[22,35] The $NiCo_2O_4$ nanoflake and nanobelt electrodes delivered a capacity of 934 and 1018 mA h g^{-1}, respectively, in the first charge process with the capacity retention ratio of around 72%. The large irreversible capacity loss in the first cycle can be ascribed to the formation of the SEI layer that cannot fully decompose during the first charge.[16] The increased capacity retention ratios of 90, 97, and 97.5% were observed in the 2nd, 50th, and 100th cycles, respectively.

Figure 8a,b shows the reversible capacities versus cycle number of the $NiCo_2O_4$ nanoflake and nanobelt electrode at the current densities of 500 and 800 mA g^{-1}. The second discharge capacities of $NiCo_2O_4$ nanoflakes and nanobelts are 1033 and 1056 mA h g^{-1}, respectively, at the current density of 500 mA g^{-1}. It is interesting to note that there is a trend of the gradual increased capacities before 40 cycles for both materials, which is ascribed to the reversible formation of a polymeric gel-like film originating from the slow kinetic activation process of the electrode. This is a general observation for transition metal oxides, and it has been well-documented in previous reports.[22,36−38] After 100 cycles, the discharge capacities are retained at 884 mA h g^{-1} for nanoflakes and 981 mA h g^{-1} for nanobelts, which are almost 85.5% and 93% of the second reversible capacities. At the high current density of 800 mA g^{-1}, the $NiCo_2O_4$ nanoflake and nanobelt electrodes still show the reversible capacity of 814 and 998 mA h g^{-1}, respectively.

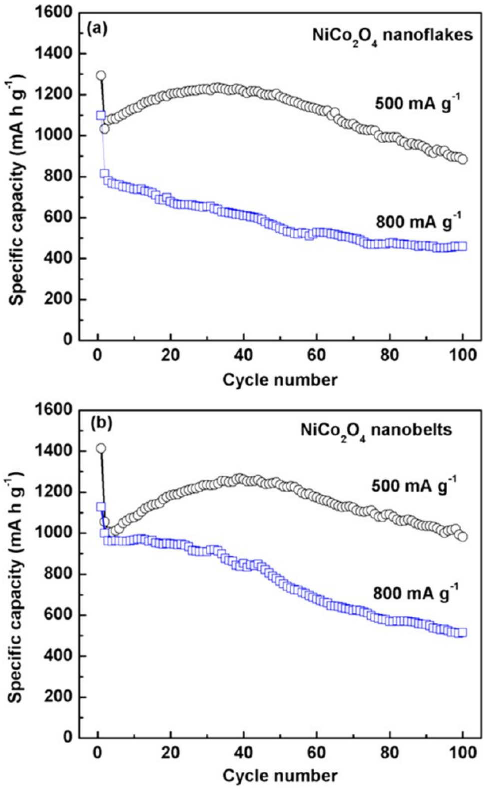

Figure 8. Cycling performance of NiCo$_2$O$_4$ electrode at the current densities of 500 and 800 mA g^{-1}: (a) nanoflakes and (b) nanobelts.

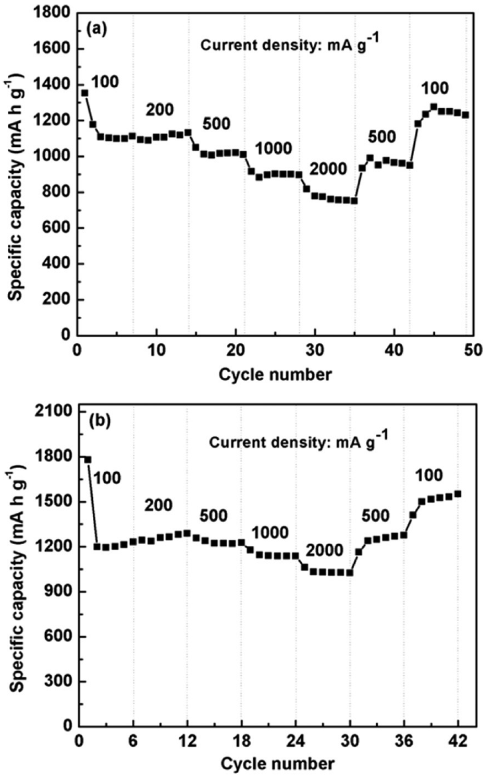

Figure 9. Rate performances for the NiCo$_2$O$_4$ electrode at various current densities: (a) nanoflakes and (b) nanobelts.

NiCo$_2$O$_4$ nanobelts exhibit better cycling stability than that of nanoflakes over 100 cycles.

The rate performances were also evaluated to investigate the high power performance of the porous NiCo$_2$O$_4$ nanoflakes and nanobelts, which is shown in Figure 9a,b. The NiCo$_2$O$_4$ nanoflake electrode was cycled at different current densities ranging from100 to 2000 mA g^{-1} (Figure 9a). The electrode shows an excellent cycling performance at differed current densities. At the current density of 2000 mA g^{-1}, the electrode still delivered a reversible capacity of 902 mA h g^{-1}. Figure 9b presents the rate capability of NiCo$_2$O$_4$ nanobelts. The nanobelt electrode also shows the capacity of 1062 mA h g^{-1}, at the high current density of 2000 mA g^{-1}. This verified the excellent rate performance of NiCo$_2$O$_4$ nanoflakes and nanobelts for high power lithium-ion batteries. Interestingly, when the currents reversed back to low current densities (500 and 100 mA g^{-1}), the discharge capacities recovered to the higher values than previous cycles for both NiCo$_2$O$_4$ nanoflakes and nanobelts. This high rate capability demonstrates that the porous NiCo$_2$O$_4$ nanoflake and nanobelt structures have potentials for high rate anodes in lithium-ion batteries. To explain the higher values than previous cycles at the low current densities, we further demonstrate SEM images of NiCo$_2$O$_4$ nanoflake and nanobelt electrodes after rate capability testing. From Figure S5a,b (Supporting Information), we can see that the NiCo$_2$O$_4$ nanoflake structure reorganized during charge—discharge cycling at different current densities and converted to nanoparticles. The nanosized particles may have provided a larger specific surface area, which effectively maximizes the NiCo$_2$O$_4$/electrolyte contact area and offers more reaction sites for Li$^+$ diffusion. Owing to the reorganization during high current density cycling, the NiCo$_2$O$_4$ nanobelt structure (Figure S5c,d) also converted to nanoparticles, providing a high specific surface area to increase the contact area between active electrode materials and electrolyte. The high contact area can provide more active sites for lithium-ion insertion/extraction. Those factors could induce the increase of specific capacity. To the best of our knowledge, reports on unique rate capabilities of porous NiCo$_2$O$_4$ nanoflakes and nanobelts are quite rare.

Electrochemical impedance spectra (EIS) were measured to understand the performance of the as-prepared porous NiCo$_2$O$_4$ nanoflakes and nanobelts. Figure 10a,b presents the Nyquist plots obtained from the NiCo$_2$O$_4$ nanoflake and nanobelt electrodes for fresh cells and after the rate capability test. Both the Nyquist plots exhibit two depressed semicircles in the high- and medium-frequency regions and a straight line in the low-frequency region. The straight line in the low-frequency region corresponds to the Warburg behavior, reflecting the solid-state diffusion of lithium ions into the bulk of the electrode materials.[39] The semicircle in the medium-frequency region is probably ascribed to the charge-transfer process. As shown in Figure 10a, there are obvious increases of charge-transfer resistance (R_{ct}) after the rate capability test for NiCo$_2$O$_4$ nanoflakes. On the other hand, the R_{ct} value of the NiCo$_2$O$_4$ nanobelt electrode (Figure 10b) is lower than that of the NiCo$_2$O$_4$ nanoflake after the rate capability test. This shows that the lithium ions and electrons can transfer more freely in the electrode/electrolyte interface and, therefore, enhance the electrode reaction kinetics and cycling stability throughout the cycling. Moreover, according to the electrochemical impedance data of the NiCo$_2$O$_4$ nanobelt electrode (Figure 10b), we can observe that the radius of the semicircle before and after the rate capability test is almost similar, demonstrating that there is no significant change in electrochemical resistance after the rate

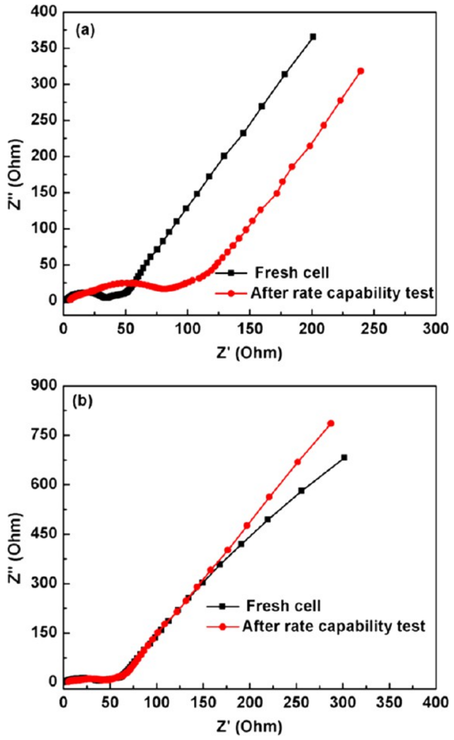

Figure 10. Electrochemical impedance spectra of the as-prepared $NiCo_2O_4$ before and after rate capability test: (a) nanoflakes and (b) nanobelts.

capability test. Furthermore, compared with the $NiCo_2O_4$ nanoflakes, the high specific surface area of porous $NiCo_2O_4$ nanobelts maximizes the contact area between active materials and electrolyte, which can provide more reaction sites.[40] Thus, $NiCo_2O_4$ nanobelts show better high specific capacity, good cycling performance, and a high rate capability than that of the $NiCo_2O_4$ nanoflakes.

The following factors could be responsible for the observed good electrochemical performance of these two materials. First, their higher specific surface area offers a large contact area between electrode and electrolyte for more Li^+ diffusion through the interface, thus improving the high specific capacity and also benefiting the charge-transfer rate, and enhancing the rate capability.[38,41] Second, the existence of pores in the $NiCo_2O_4$ nanoflakes and nanobelts could cushion the volume change associated with the Li^+ intercalation/deintercalation process during the long-term charge−discharge cycling and alleviate the aggregation and pulverization of the electrode material, thereby improving cycling stability.

4. CONCLUSIONS

We established a facile hydrothermal method to produce both $NiCo_2O_4$ nanoflakes and $NiCo_2O_4$ nanobelts, followed by annealing in air. The materials have a high specific surface area and a mesoporous structure, which facilitate the fast transportation of Li^+ and also accommodate the volume variation based on the conversion reaction during the charge/discharge process. When applied as an anode material for LIB applications, the $NiCo_2O_4$ nanoflake and nanobelt electrodes retained reversible capacities of 884 and 981 mA h g^{-1}, respectively, at the current density of 500 mA g^{-1}, even after 100 cycles, which is 85.5% and 93% of the second discharge capacities. When the $NiCo_2O_4$ nanoflake and nanobelt electrodes were cycled at different current densities (100−2000 mA g^{-1}), both the materials still delivered the capacity of 902 and 1062 mA h g^{-1}, respectively, even at a high current density of 2000 mA g^{-1}, demonstrating an excellent high rate capability. The simple preparation process and excellent electrochemical performances render porous $NiCo_2O_4$ nanoflakes and nanobelts to be attractive anode materials for lithium-ion batteries.

■ ASSOCIATED CONTENT

Ⓢ Supporting Information

SEM of precursors ($NiCo_2O_4$ nanoflakes and nanobelts), SEM-EDX pattern, TGA curves, FTIR spectra, and SEM images of the $NiCo_2O_4$ nanoflakes and nanobelts after rate capability test. This material is available free of charge via the Internet at http://pubs.acs.org.

■ AUTHOR INFORMATION

Corresponding Authors

*E-mail: anjonmondal@yahoo.com. Phone: +61 02 9514 8244. Fax: +61 02 9514 1656 (A. K. Mondal).
*E-mail: Guoxiu.Wang@uts.edu.au. Phone: +61 02 9514 1741. Fax: +61 02 9514 1656 (G. Wang).

Notes

The authors declare no competing financial interest.

■ ACKNOWLEDGMENTS

The authors gratefully acknowledge the financial support provided by the Australian Research Council (ARC) through the ARC discovery project (DP1093855).

■ REFERENCES

(1) Wang, X. D.; Song, J. H.; Liu, J.; Wang, Z. L. Direct-Current Nanogenerator Driven by Ultrasonic Waves. *Science* **2007**, *316*, 102−105.

(2) Xia, C. R.; Liu, M. L. Novel Cathodes for Low-Temperature Solid Oxide Fuel Cells. *Adv. Mater.* **2002**, *14*, 521−523.

(3) Tian, B.; Zheng, X. T.; Kempa, J.; Fang, Y.; Yu, N.; Yu, G.; Huang, J.; Lieber, C. M. Coaxial Silicon Nanowires as Solar Cells and Nanoelectronic Power Sources. *Nature* **2007**, *449*, 885−889.

(4) Bruce, P. G.; Scrosati, B. J.; Tarascon, M. Nanomaterials for Rechargeable Lithium Batteries. *Angew. Chem., Int. Ed.* **2008**, *47*, 2930−2946.

(5) Arico, S.; Bruce, P.; Scrosati, B.; Tarascon, J. M.; Van, S. W. Nanostructured Materials for Advanced Energy Conversion and Storage Devices. *Nat. Mater.* **2005**, *4*, 366−377.

(6) Kim, M. G.; Cho, J. Reversible and High-Capacity Nanostructured Electrode Materials for Li-Ion batteries. *Adv. Funct. Mater.* **2009**, *19*, 1497−1514.

(7) Poizot, P.; Laruelle, S.; Grugeon, S.; Dupont, L.; Tarascon, J. M. Nano-sized Transition-Metal Oxides as Negative-Electrode Materials for Lithium-Ion Batteries. *Nature* **2000**, *407*, 496−499.

(8) Cheng, F. Y.; Wang, H. B.; Zhu, Z. Q.; Wang, Y.; Zhang, T. R.; Tao, Z. L.; Chen, J. Porous $LiMn_2O_4$ Nanorods with Durable High-Rate Capability for Rechargeable Li-Ion Batteries. *Energy Environ. Sci.* **2011**, *4*, 3668−3675.

(9) Li, W. Y.; Xu, L. N.; Chen, J. Nanomaterials in Lithium-Ion Batteries and Gas Sensors. *Adv. Funct. Mater.* **2005**, *15*, 851−857.

(10) Liu, J.; Xia, H.; Xue, D.; Lu, L. Double-Shelled Nanocapsules of V_2O_5-Based Composites as High-Performance Anode and Cathode Materials for Li Ion Batteries. *J. Am. Chem. Soc.* **2009**, *131*, 12086−12087.

(11) Ci, S.; Zou, J.; Zeng, G.; Peng, Q.; Luo, S.; Wen, Z. Improved Electrochemical Properties of Single Crystalline NiO Nanoflakes for

Lithium Storage and Oxygen Electroreduction. *RSC Adv.* **2012**, *2*, 5185−5192.

(12) Zhang, J.; Huang, T.; Liu, Z.; Yu, A. Mesoporous Fe_2O_3 Nanoperticles as High Performance Anode Materials for Lithium-Ion Batteries. *Electrochem. Commun.* **2013**, *29*, 17−20.

(13) Sharma, Y.; Sharma, N.; Rao, G. V. S.; Chowdari, V. V. R. Lithium Recycling Behaviour of Nano-phase-$CuCo_2O_4$ as Anode for Lithium-Ion Batteries. *J. Power Sources* **2007**, *173*, 495−501.

(14) Li, J. F.; Xiong, S. L.; Li, X. W.; Qian, Y. T. A Facile Route to Synthesize Multiporous $MnCo_2O_4$ and $CoMn_2O_4$ Spinel Quasi-Hollow Spheres with Improved Lithium Storage Properties. *Nanoscale* **2013**, *5*, 2045−2054.

(15) Qiu, Y.; Yang, S.; Deng, H.; Jin, L.; Li, W. A Novel Nanostructured Spinel $ZnCo_2O_4$ Electrode Material: Morphology Conserved Transformation from a Hexagonal Shaped Nanodisk Precursor and Application in Lithium Ion Batteries. *J. Mater. Chem.* **2010**, *20*, 4439−4444.

(16) Li, J. F.; Xiong, S. L.; Liu, Y.; Ju, Z.; Qian, Y. T. High Electrochemical Performance of Monodisperse $NiCo_2O_4$ Mesoporous Microspheres as an Anode Material for Li-Ion Batteries. *ACS Appl. Mater. Interfaces* **2013**, *5*, 981−988.

(17) Zhou, L.; Wu, H. B.; Zhu, T.; Lou, X. W. Facile Preparation of $ZnMn_2O_4$ Hollow Microspheres as High-Capacity Anodes for Lithium-Ion Batteries. *J. Mater. Chem.* **2012**, *22*, 827−829.

(18) Wei, T. Y.; Chen, C. H.; Chien, H. C.; Lu, S. Y.; Hu, C. C. A Cost-Effective Supercapacitor Material of Ultrahigh Specific Capacitances: Spinel Nickel Cobaltite Aerogels from an Epoxide-Driven Sol-Gel Process. *Adv. Mater.* **2010**, *22*, 347−351.

(19) Hu, L. F.; Wu, L. M.; Liao, M. Y.; Fang, X. S. High-Performance $NiCo_2O_4$ Nanofilm Photodetectors Fabricated by an Interfacial Self-Assembly Strategy. *Adv. Mater.* **2011**, *23*, 1988−1992.

(20) Li, Y. G.; Hasin, P.; Wu, Y. Y. Nanowire Arrays for Electrocatalytic Oxygen Evolution. *Adv. Mater.* **2010**, *22*, 1926−1929.

(21) Jiang, H.; Ma, J.; Li, C. Hierarchical Porous $NiCo_2O_4$ Nanowires for High-Rate Supercapacitors. *Chem. Commun.* **2012**, *48*, 4465−4467.

(22) Li, L.; Cheah, Y.; Ko, Y.; Teh, P.; Wee, G.; Wong, C.; Peng, S.; Srinivasan, M. The Facile Synthesis of Hierarchical Porous Flower-like $NiCo_2O_4$ with Superior Lithium Storage Properties. *J. Mater. Chem. A* **2013**, *1*, 10935−10941.

(23) Fang, X.; Yu, X.; Liao, S.; Shi, Y.; Hu, Y. S.; Wang, Z.; Stucky, G. D. Lithium Storage Performance in Ordered Mesoporous MoS_2 Electrode Material. *Microporous Mesoporous Mater.* **2012**, *151*, 418−423.

(24) Liu, H.; Wang, G.; Liu, X. J.; Qiao, S. Z.; Ahn, H. Highly Ordered Mesoporous NiO Anode Material for Lithium Ion Batteries with an Excellent Electrochemical Performance. *J. Mater. Chem.* **2011**, *21*, 3046−3052.

(25) Li, L.; Peng, S.; Cheah, Y.; Teh, P.; Wang, J.; Wee, G.; Ko, Y.; Wong, C.; Srinivasan, M. Electrospun Porous $NiCo_2O_4$ Nanotubes as Advanced Electrodes for Electrochemical Capacitors. *Chem.—Eur. J.* **2013**, *19*, 5892−5898.

(26) Wang, Q.; Wang, X.; Liu, B.; Yu, G.; Hou, X.; Chen, D.; Shen, G. $NiCo_2O_4$ Nanowire Arrays Supported on Ni Foam for High Performance Flexible All-Solid-State Supercapacitors. *J. Mater. Chem. A* **2013**, *1*, 2468−2473.

(27) Ding, R.; Qi, L.; Wang, H. A Facile and Cost-Effective Synthesis of Mesoporous $NiCo_2O_4$ Nanoparticles and Their Capacitive Behaviour in Electrochemical Capacitors. *J. Solid State Electrochem.* **2012**, *16*, 3621−3633.

(28) Yuan, C.; Li, J.; Hou, L.; Zhang, X.; Shen, L.; Lou, X. W. Ultrathin Mesoporous $NiCo_2O_4$ Nanosheets Supported on Ni Foam as Advanced Electrodes for Supercapacitors. *Adv. Funct. Mater.* **2012**, *22*, 4592−4597.

(29) Liu, J.; Liu, C.; Wan, Y.; Liu, W.; Ma, Z.; Ji, S.; Wang, J.; Zhou, Y.; Hodgson, P.; Li, Y. Facile Synthesis of $NiCo_2O_4$ Nanorod Arrays on Cu Conductive Substrates as Superior Anode Materials for High-Rate Li-Ion Batteries. *CrystEngComm.* **2013**, *15*, 1578−1585.

(30) Vinu, A.; Sawant, D. P.; Ariga, K.; Hartmann, M.; Halligudi, S. B. Benzylation of Benzene and Other Aromatics by Benzyl Chloride over Mesoporous AlSBA-15 Catalysts. *Microporous Mesoporous Mater.* **2005**, *80*, 195−203.

(31) Guan, H.; Shao, C.; Liu, Y.; Yu, N.; Yang, X. Fabrication of $NiCo_2O_4$ Nanofibers by Electrospinning. *Solid State Commun.* **2004**, *131*, 107−109.

(32) Liu, L.; Li, Y.; Yuan, S. M.; Ge, M.; Ren, M. M.; Sun, C. S.; Zhou, Z. Nanosheet-Based NiO Microspheres: Controlled Solvothermal Synthesis and Lithium Storage Performances. *J. Phys. Chem. C* **2010**, *114*, 251−255.

(33) Xiong, S. L.; Chen, J. S.; Loo, X. W.; Zeng, H. C. Mesoporous Co_3O_4 and CoO@C Topotactically Transformed from Chrysanthemum-like $Co(CO_3)_{0.5}(OH)$ Center Dot $0.11H_2O$ and Their Lithium-Storage Properties. *Adv. Funct. Mater.* **2012**, *22*, 861−871.

(34) Chen, Y.; Zhuo, M.; Deng, J.; Xu, Z.; Li, Q.; Wang, T. Reduced Graphene Oxide Networks as an Effective Buffer Matrix to Improve the Electrode Performance of Porous $NiCo_2O_4$ Nanoplates for Lithium-Ion Batteries. *J. Mater. Chem. A* **2014**, *2*, 4449−4456.

(35) Hu, L.; Zhong, H.; Zheng, X. R.; Huang, Y. M.; Zhang, P.; Chen, Q. W. $CoMn_2O_4$ Spinel Hierarchical Microspheres Assembled with Porous Nanosheets as Stable Anodes for Lithium-Ion Batteries. *Sci. Rep.* **2012**, *2*, 986.

(36) Do, J. S.; Weng, C. H. Preparation and Characterization of CoO Used as Anodic Material of Lithium Battery. *J. Power Sources* **2005**, *146*, 482−486.

(37) Grugeon, S.; Laruelle, S.; Dupont, L.; Tarascon, J. M. An Update on the Reactivity of Nanoparticles Co-based Compounds towards Li. *Solid State Sci.* **2003**, *5*, 895−904.

(38) Li, J.; Xiong, S.; Li, X.; Qian, Y. Spinel $Mn_{1.5}Co_{1.5}O_4$ Core-Shell Microspheres as Li-Ion Battery Anode Material with a Long Cycle Life and High Capacity. *J. Mater. Chem.* **2012**, *22*, 23254−23259.

(39) Shaju, K. M.; Jiao, F.; Debart, A.; Bruce, P. G. Mesoporous and Nanowire Co_3O_4 as Negative Electrodes for Rechargeable Lithium Batteries. *Phys. Chem. Chem. Phys.* **2007**, *9*, 1837−1842.

(40) Tian, L.; Zou, H. L.; Fu, J. X.; Yang, X. F.; Yang, Y.; Guo, H. L.; Fu, X. H.; Liang, C. L.; Wu, M. M.; Shen, P. K.; Gao, M. Q. Topotactic Conversion Route to Mesoporous Quasi-Single-Crystalline Co_3O_4 Nanobelts with Optimizable Electrochemical Performance. *Adv. Funct. Mater.* **2010**, *20*, 617−623.

(41) Liu, D.; Cao, G. Engineering Nanostructured Electrodes and Fabrication of Film electrodes for Efficient Lithium Ion Intercalation. *Energy Environ. Sci.* **2010**, *3*, 1218−1237.

(42) Chen, Y.; Zhu, J.; Qu, B.; Lu, B.; Xu, Z. Graphene Improving Lithium-Ion Battery Performance by Construction of $NiCo_2O_4$/Graphene Hybrid Nanosheet Arrays. *Nano Energy* **2014**, *3*, 88−94.

(43) Reddy, M. V.; Rao, G. V. S.; Chowdari, B. V. R. Metal Oxides and Oxysalts as Anode Materials for Li Ion Batteries. *Chem. Rev.* **2013**, *113*, 5364−5457.

(44) Dedryvere, R.; Foix, D.; Franger, S.; Patoux, S.; Daniel, L.; Gonbeau, D. Electrode/Electrolyte Interface Reactivity in High-Voltage Spinel $LiMn_{1.6}Ni_{0.4}O_4/Li_4Ti_5O_{12}$ Lithium-Ion Battery. *J. Phys. Chem. C* **2010**, *114*, 10999−11008.